Mixed crystal formation and structural studies in the mullite-type system Bi$_2$Fe$_4$O$_9$–Bi$_2$Mn$_4$O$_{10}$

Zachary R. Kann [a], Jeffrey T. Auletta [a], Eric W. Hearn [a], Sven-U. Weber [b], Klaus D. Becker [b], Hartmut Schneider [c], Michael W. Lufaso [a],*

[a] Department of Chemistry, University of North Florida, 1 UNF Drive, Jacksonville, FL 32224, USA
[b] Institute of Physical and Theoretical Chemistry, Technische Universität Braunschweig, D-38106 Braunschweig, Germany
[c] Institute of Crystallography, Universität zu Köln, 50939 Köln, Germany

ARTICLE INFO

ABSTRACT

The limits of metal cation substitution and distribution in the sequence Bi$_2$Fe$_4$O$_9$–Bi$_2$Mn$_4$O$_{10}$ have been investigated by solid state synthesis, X-ray powder diffraction, and Mössbauer spectroscopy. Rietveld refinements conducted for the entire range along the join indicate the structures are orthorhombic with space group $Pbam$, with partial transition-metal site disorder confirmed and detailed by Mössbauer spectroscopy. Single-phase regions are found near each end-member and a two-phase region is observed at intermediate compositions, extending from about $x=1$ to 3, according to the general formula of the mixed crystals Bi$_2$Fe$_{4-x}$Mn$_x$O$_{10-\delta}$. An incorporation of Mn at octahedral sites replacing Fe is taken into account for the Bi$_2$Fe$_4$O$_9$-related side of the system. Charge compensation is believed to be effected by addition of O, which gives rise to the formation of FeO$_5$ pyramids. At the Bi$_2$Mn$_4$O$_{10}$-related side of the system, substitution of pyramidal Mn^{3+} by Fe^{3+} is envisaged.

1. Introduction

Bismuth-containing metal oxides in the Bi$_2$Mn$_4$O$_{10}$ and Bi$_2$M$_4$O$_9$ (M=Al, Ga, Fe) family have been the subject of considerable study because of fundamentally interesting structural, magnetic, and electrical properties. Research has continued on these compounds, not only because of interesting structure and properties, but also because of potential applications including electrolytes in solid oxide fuel cells [1,2], gas sensors [3], oxygen sensors [4], chemical catalysts [5], photocatalysts [6,7], magneto-electric coupling systems [8], and as multiferroic [9] oxides with new functionalities [10].

The crystal structures of compounds of composition Bi$_2$M$_4$O$_9$ (M=Al, Ga, Fe) [11–13] and Bi$_2$M$_4$O$_{10}$ (M=Mn) [14,15] have been examined in several previous studies. The end members of the mixed crystal series, Bi$_2$Mn$_4$O$_{10}$ and Bi$_2$Fe$_4$O$_9$, belong to the family of mullite-type structures [16]. Both compounds have the same space group ($Pbam$) and differ by only one oxygen atom [12,16]. Each structure contains the mullite-type edge-sharing columns of MO$_6$ octahedra aligned parallel to the c-axis. The columns are linked by apex-sharing MO$_4$ (M=Al, Ga, Fe) tetrahedra or edge-sharing MO$_5$ (M=Mn) distorted tetragonal pyramids, respectively. Bismuth ions, located between the columns, are surrounded by six (Bi$_2$M$_4$O$_9$) or eight (Bi$_2$M$_4$O$_{10}$) oxygen atoms. The polarizable 6s^2 lone electron pairs point toward vacant sites in the crystal structure of Bi$_2$M$_4$O$_9$, whereas Bi$_2$M$_4$O$_{10}$ seems not to contain stereochemically active 6s^2 lone electron pairs; since Bi^{3+} can easily be replaced by REE^{3+} (REE=rare earth element) and Y^{3+}, having no lone electron pairs. A comparison of the two structures is shown in Fig. 1. The O1, as part of the corner-sharing tetrahedron in the Bi$_2$M$_4$O$_9$ structure and the edge-sharing tetragonal pyramid in the Bi$_2$Mn$_4$O$_{10}$ structure, is highlighted to illustrate the primary difference in the structures.

Previous studies investigated site substitutions on both the Bi- and M-sites [17], where solid solutions were reported for Bi$_{2-x}$Sr$_x$Al$_4$O$_{9-\delta}$ [18], Bi$_{1.8}$Ba$_{0.2}$Mn$_4$O$_{10}$ [19], Bi$_{1.8}$Ce$_{0.2}$Mn$_4$O$_{10}$ (and a large number of phases where Bi^{3+} is partially or fully replaced by Y^{3+} or threefold charged rare earth cations) [20], Bi$_2$Fe$_{4-x}$Ga$_x$O$_9$ [21], Bi$_2$Mn$_{4-x}$Ti$_x$O$_{10}$ [22], Bi$_2$Fe$_{4-x}$Cr$_x$O$_9$ [23], and Bi$_2$Fe$_{4-x}$Al$_x$O$_9$ [24]. There are significant differences and conflicting reports about the substitution limits and the crystallographic sites the Mn and Fe cations occupy in Bi$_2$Fe$_{4-x}$Mn$_x$O$_{10-\delta}$ [25–29]. The limits were reported by Masuno to exist from $0 \leq x \leq 0.9$ for the Bi$_2$Fe$_4$O$_9$-type phase, $3.6 \leq x \leq 4$ for the Bi$_2$Mn$_4$O$_{10}$ type phase, and the existence of a multiphase region for $0.9 < x < 3.6$ [25]. Subsequently, Jimenez reported that both compounds crystallize in the orthorhombic system and dissolve in all proportions, but
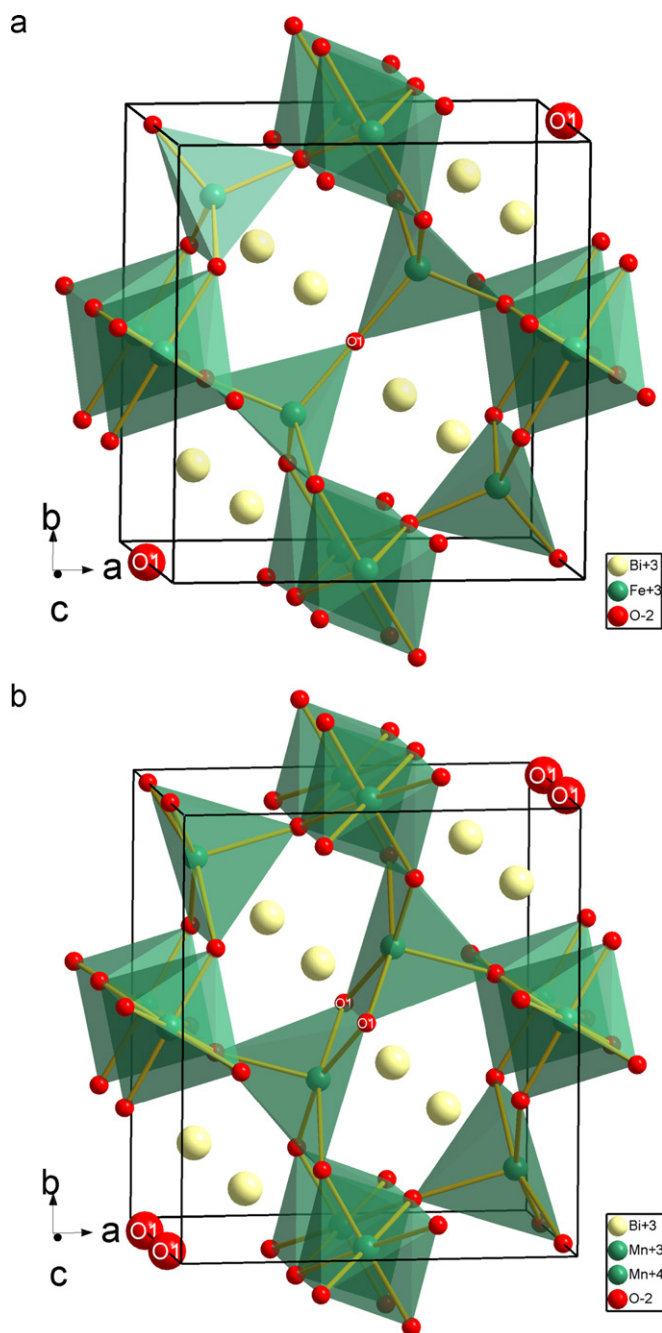
Fig. 1. Crystal structure of (a) $Bi_2Fe_4O_9$ and (b) $Bi_2Mn_4O_{10}$. Note that the octahedral chains in $Bi_2Fe_4O_9$ are linked by dimers of tetrahedra, whereas they are linked by dimers of pyramids in the case of $Bi_2Mn_4O_{10}$.

presented some deviations from Vegard's Law [26]. Single-crystal X-ray diffraction data of a flux-grown single crystal of $Bi_2Mn_2Fe_2O_{10}$ was reported by zur Loye which, as the intermediate $x=2$ member, supports the possibility for a complete solid solution, at least between $Bi_2Mn_4O_{10}$ and $Bi_2Fe_2Mn_2O_{10}$ [27]. Nguyen et al. subsequently reported miscibility exists along the $3 \leq x \leq 4$ region, but noted they were unable to prepare $Bi_2Mn_2Fe_2O_{10}$ using conventional synthesis [28]. A recent examination of the ternary phase diagram for Bi–Fe–Mn–O reported no solid solution along the sequence $Bi_2Fe_4O_9$–$Bi_2Mn_4O_{10}$ [29].

The slow solid-state kinetics at low synthesis temperature, similar crystal structures of the two end members, and peak overlap may have led to complexity in interpreting the X-ray diffraction data. The differences reported in previous studies led

us to thoroughly examine the substitution limits using solid-state synthesis, X-ray powder diffraction, and Mössbauer spectroscopy. In this contribution, we report a detailed analysis of the phase stability range, structure, and cation distribution in the sequence $Bi_2Fe_4O_9$–$Bi_2Mn_4O_{10}$.

2. Experimental

Samples were synthesized by solid-state reaction in air using stoichiometrically-weighed oxides of Bi_2O_3 (99.975%), MnO_2 (99.9%), and Fe_2O_3 (99.945%). Reactants were ground using an agate mortar and pestle under acetone, then heated at 725–775 °C in a high-form alumina crucible to minimize the initial possibility for loss of bismuth oxide. Subsequently, and with intermediate grinding, samples were heated at increasing temperatures up to 825 °C. Samples were analyzed by X-ray powder diffraction (XRD) using a Rigaku Ultima III X-ray diffractometer with Cu$K\alpha$ radiation. Equilibrium was assumed when no shift or change in intensity of the weakest peaks from the XRD pattern was observed. The number of heating cycles generally took four or more to approach equilibrium. The structures were refined using the Rietveld technique and the FULLPROF software program [30].

Mössbauer spectra of selected polycrystalline samples of the $Bi_2Fe_4O_9$–$Bi_2Mn_4O_{10}$ system were recorded at room temperature with a conventional microcomputer-controlled spectrometer (Halder) in sinusoidal mode. ^{57}Co/Rh radiation sources were of maximum activity of 1.8 GBq at the time of the experiments. The transmitted intensities were stored in a 1024 multichannel analyzer (Halder). The Mössbauer spectra were folded and fitted with the Recoil Mössbauer analysis program [31] using Voigt-type lineshapes accounting for the distribution of quadrupolar interactions, and decomposed into subspectra with parameters of the following meaning: isomer-shift (IS) relative to α-Fe (mm/s), width Γ of the Lorentzian contribution to the lineshape (mm/s), quadrupole splitting (QS) (mm/s), σ_{QS} width of quadrupolar distribution, and area (A) (%) of the different subspectra.

3. Results

3.1. X-ray diffraction

The ambient temperature X-ray diffraction patterns for a representative set of samples in the sequence are shown in Fig. 2. Preliminary analysis indicated the X-ray diffraction patterns of the end members could be indexed on the basis of an orthorhombic unit cell in space group *Pbam*, in agreement with earlier studies [12,15]. Indexing using a single phase could not be completed with a suitable unit cell for some intermediate compositions (e.g. $x=2$ in $Bi_2Fe_{4-x}Mn_xO_{10-\delta}$).

The difference in lattice parameters of the end members enable the use of the 201 peak near 27°2θ and the 211 peak near 28°2θ to initially distinguish between the two phases, although care must be taken when the amount of the minority phase is small. In order to deal with weak and overlapping peaks and accurately determine the presence of a single phase or two phases, Rietveld refinements were conducted for all samples. A two-phase refinement was conducted if the diffraction pattern showed evidence for a second phase and was poorly fit using a single phase.

Starting structure models were obtained using the crystal structures of the $Bi_2Fe_4O_9$ and $Bi_2Mn_4O_{10}$ end members [12,15]. Refinements rapidly converged with close agreement to the reported structures in the literature. For intermediate compositions, the cation distribution for each transition metal site was
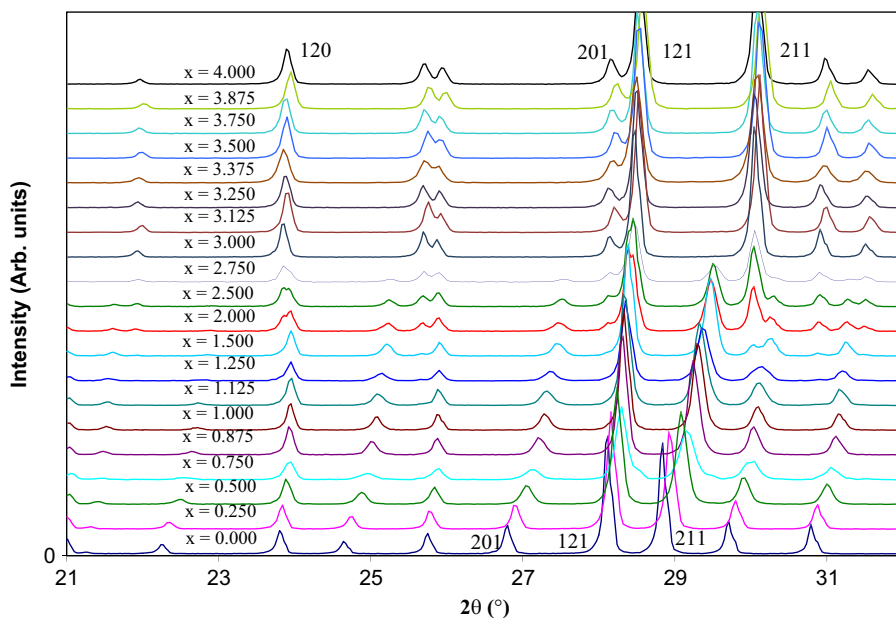
Fig. 2. XRD patterns of selected samples in the sequence from 22° to 32°2θ. The progression goes from $Bi_2Fe_4O_9$ ($x=0$) at the bottom to $Bi_2Mn_4O_{10}$ ($x=4$) at the top.
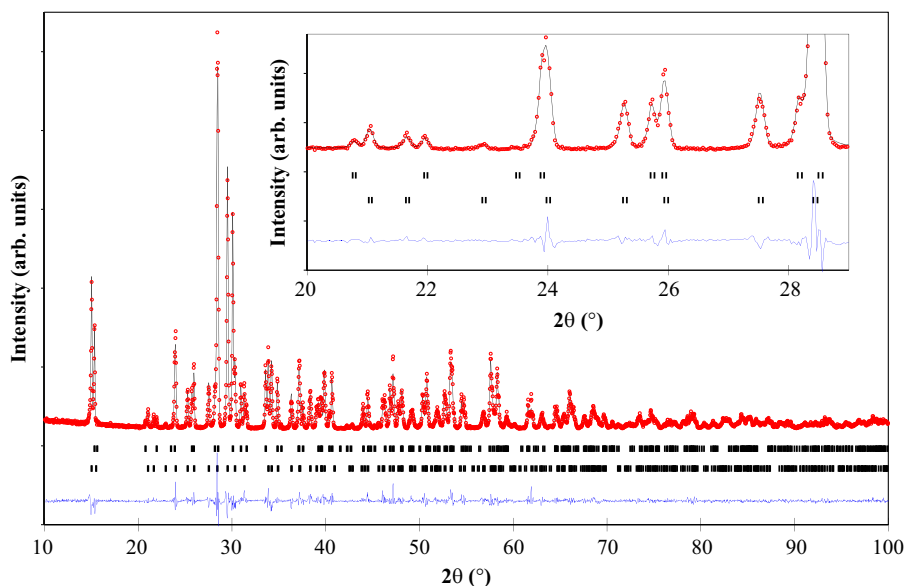

Fig. 3. Observed X-ray diffraction pattern along with calculated and difference pattern from Rietveld refinement of a sample prepared at the $x=2$ composition. The upper and lower sets of tick marks indicate the expected 2θ positions of the peaks for the $Bi_2Fe_4O_9$-type and $Bi_2Mn_4O_{10}$-type phase, respectively.

initially fixed at the overall composition of the sample for the initial stages of the structure refinements, with the Fe and Mn cations were assumed to equally share both the tetragonal pyramidal and octahedral sites in the $Bi_2Mn_4O_{10}$-type model and in the $Bi_2Fe_4O_9$-type model the Fe and Mn cations assumed to equally share both tetrahedral and octahedral sites. The similar electron density for the iron and manganese cations result in an inability to meaningfully refine the Fe and Mn cation distribution between the two sites, since the laboratory X-ray data is insensitive to minor changes in electron density. However, the cations exhibit a site preference, see below in the Mössbauer section.

The X-ray diffraction pattern and refined crystal structures for a sample prepared at the $x=2$ composition are shown in Fig. 3. A satisfactory fit to the experimental data is only obtained using a two-phase Rietveld refinement, confirming the inability to prepare $Bi_2Mn_2Fe_2O_{10}$ using the conditions of the conventional solid state

synthesis technique in this study. Details of the refined structural parameters are available in the Supplementary Information.

The results from Rietveld refinements of all samples along the series indicate the solid solution limits extend from $0 \leq x < 0.875$ in $Bi_2Fe_{4-x}Mn_xO_{9+\delta}$ and from $3.125 \leq x \leq 4$ in $Bi_2Fe_{4-x}Mn_xO_{10}$. The mass fraction of the two phases was refined and the mass fraction of the $Bi_2Mn_4O_{10}$-type phase versus composition obtained from the Rietveld refinements of samples prepared at 825 °C is shown in Fig. 4.

The amount of a secondary phase at the $x=3$ composition, $Bi_2FeMn_3O_{10}$, decreased with subsequent annealing and the sample was slow to approach equilibrium at 825 °C, requiring multiple heat cycles with intermediate grinding to approach equilibrium. A possible reason for the minor differences in the solid solution limits reported in different studies may arise from different synthesis temperatures, e.g. 850 °C used by Nguyen et al. [28],
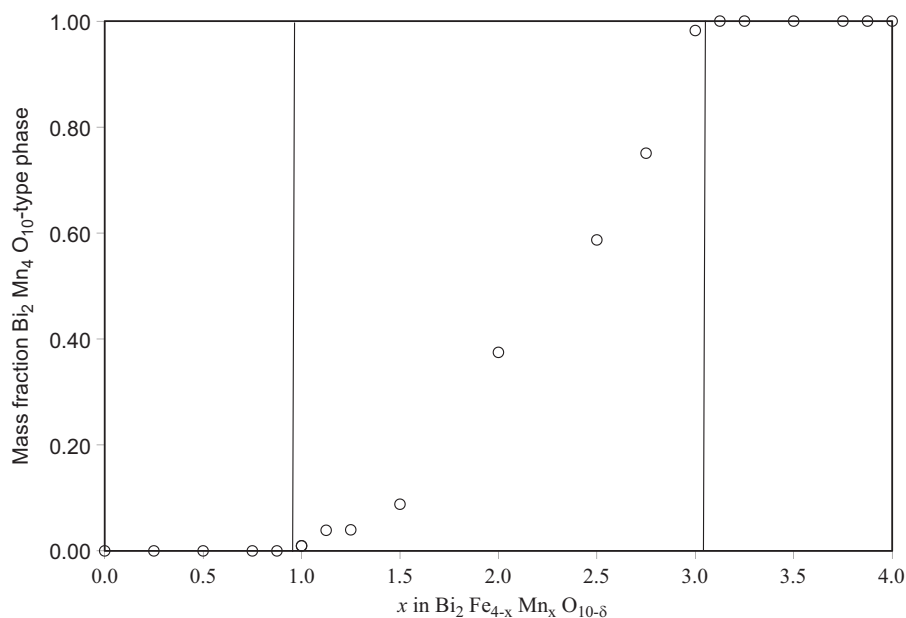
Fig. 4. Mass fraction of $Bi_2Mn_4O_{10}$-type phase as a function of composition (x) in $Bi_2Fe_{4-x}Mn_xO_{10-\delta}$ obtained from Rietveld refinements. Vertical guide lines separate single phase and two phase regions.
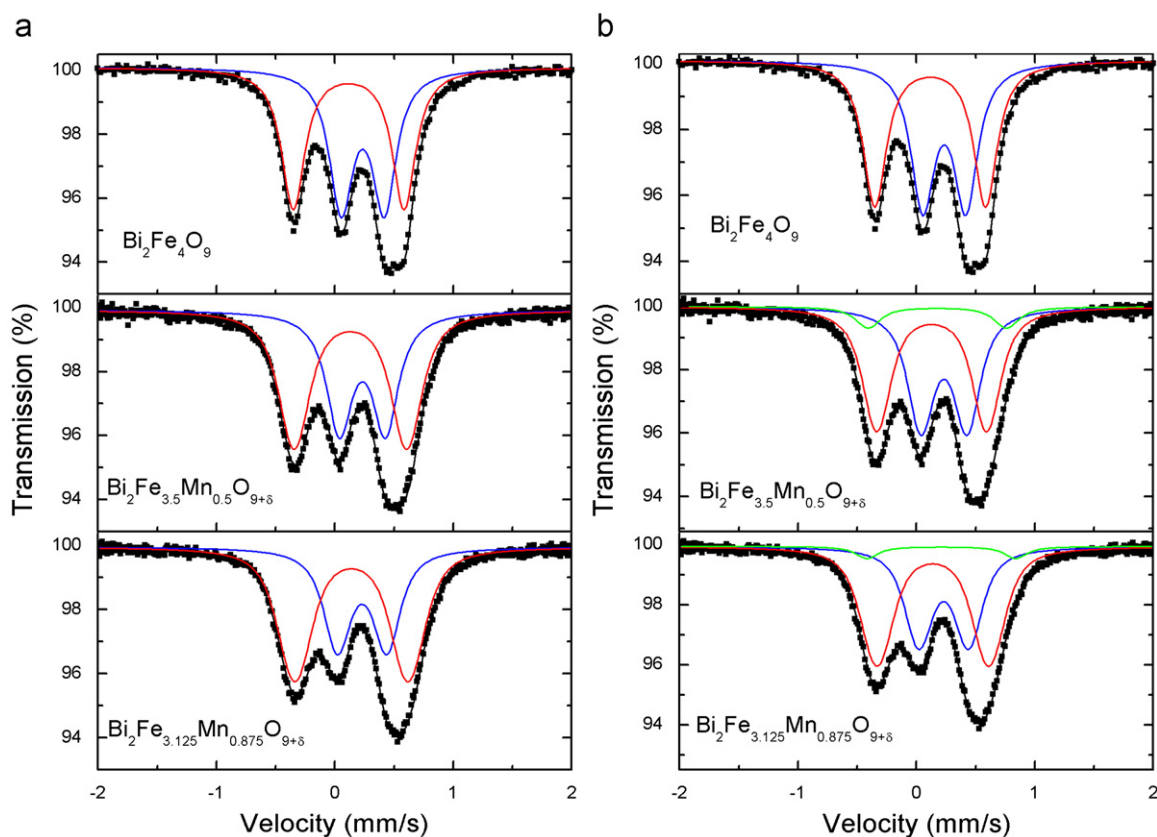
Fig. 5. (a) ^{57}Fe-Mössbauer room temperature spectra of selected compositions in $Bi_2Fe_{4-x}Mn_xO_9$-type, $x=0$, 0.5, 0.875 assuming two different iron species. The blue lines represented the doublet assigned to octahedrally coordinated Fe^{3+} and the red lines represented the doublet assigned to tetrahedrally coordinated Fe^{3+}. (b) ^{57}Fe-Mössbauer room temperature spectra of selected compositions in $Bi_2Fe_{4-x}Mn_xO_9$-type, $x=0$, 0.5, 0.875 assuming three different iron species. The blue lines represented the doublet assigned to octahedrally coordinated Fe^{3+}, the red lines represented the doublet assigned to tetrahedrally coordinated Fe^{3+}, and the green lines represented the doublet assigned to tetragonal-pyramidally coordinated Fe^{3+}. (For interpretation of the references to color in this figure legend, the reader is referred to the web version of this article.)

compared to observed solid solution limits at 825 °C in this study. After annealing at 850 °C, the $x=3$ sample is single phase in agreement with the previous report [28]. At temperatures

above 850 °C we observed well-sintered pellets, evidence for liquid phase formation, secondary perovskite-related phases (i.e. $BiFeO_3$), and broadening of the Bragg reflections for some

samples. Similar observations to our results were recently reported in the formation of $BiMnO_3$ as a secondary phase during the sintering of $Bi_{1.8}Ba_{0.2}Mn_4O_{10}$ at high temperature [19].

3.2. Mössbauer spectroscopy

Local coordination environment information is provided by Mössbauer spectroscopy and is an additional probe to complement the analysis by X-ray diffraction data. Mössbauer spectra of selected $Bi_2Fe_{4-x}Mn_xO_9$-type solid solutions with $0 \leq x \leq 0.875$ are shown in Fig. 5a and b. Two structure models were used in the analysis, the first assuming two different iron species (Fig. 5a) and the second assuming three different iron species (Fig. 5b). The spectra of the mixed crystals are similar to that of the iron end member of the solid solution ($x=0$) [24,32]. Spectra are given by a superposition of two quadrupolar doublets due to Fe^{3+} of similar intensity where the subspectrum with the smaller splitting and the larger isomer shift is attributed to octahedrally coordinated iron (Table 1). The data show a mixed site occupancy where the fraction of iron cations in the non-octahedral coordinated sites increases with increasing manganese content of the solid solution. The present Mössbauer data show that the non-octahedral sites in $Bi_2Fe_{4-x}Mn_xO_{9+\delta}$ are primarily filled by iron with close to two Fe^{3+} per formula unit and that, consequently, the manganese cations ions are primarily incorporated on octahedral sites in the $Bi_2M_4O_9$-type structure.

Fig. 6 shows selected spectra of solid solutions of the $Bi_2M_4O_{10}$-type for $3 \leq x < 4$. Spectra can be described by superposition of two quadrupolar doublets with, however, significantly different intensities. The spectra are dominated by the subspectrum due to iron in the tetragonal pyramidally coordinated sites. Thus, also in this phase, iron cations are found to clearly prefer the site that is not octahedrally coordinated by oxygen. For $x \rightarrow 4$, the fraction of iron located on the tetragonal pyramidal site increases up to about 90% (Fig. 7). As evidenced by the isomer shift, iron is trivalent in the $Bi_2M_4O_{10}$-type structure.

4. Discussion

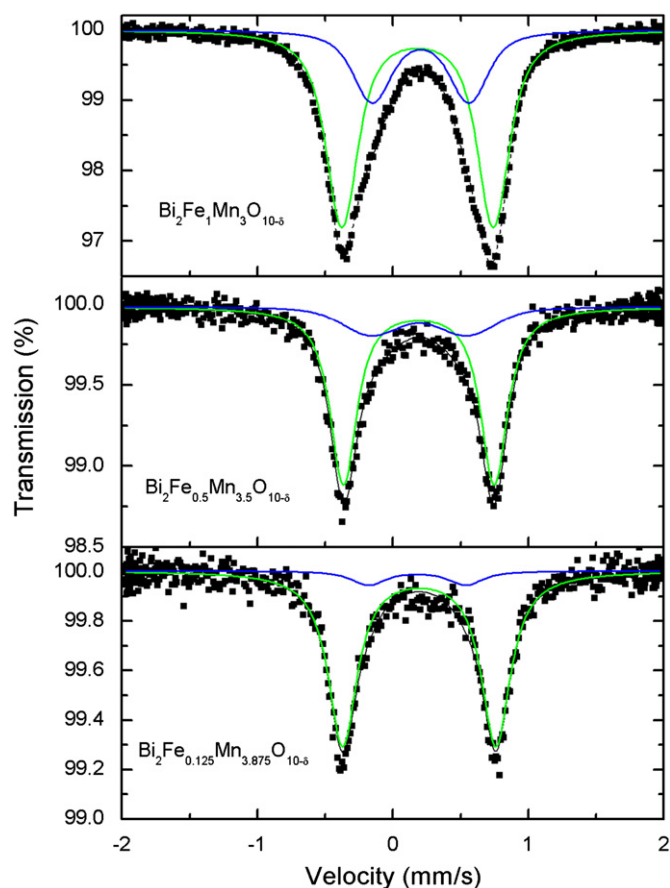### 4.1. Mixed crystal formation in the system $Bi_2Fe_4O_9$–$Bi_2Mn_4O_{10}$

As indicated in Fig. 4, there are three distinct regions within the system $Bi_2Fe_{4-x}Mn_xO_{10-\delta}$ synthesized at 825 °C: (i) single-phase $Bi_2Mn_4O_{10}$-type $\approx 3.125 \leq x < 4$, (ii) single-phase $Bi_2Fe_4O_9$-type $0 \leq x < \approx 0.875$, and (iii) two-phase $Bi_2Fe_4O_9$-type and $Bi_2Mn_4O_{10}$-type $\approx 1 \leq x \leq \approx 3$. As the amount of Mn is substituted in place of Fe into $Bi_2Fe_4O_9$, a solid solution limit is reached in the $Bi_2Fe_4O_9$-type structure, and similarly a limited amount of Fe can be substituted in place of Mn and retain the $Bi_2Mn_4O_{10}$ type structure. In the intermediate zone, a wide two-phase region exists. The unit cell volumes versus composition of the samples synthesized at 825 °C are given in Fig. 8. The amounts of the two different phases vary as shown in Fig. 4, but it is not a simple variation based solely on the relative amounts of the two solid solution limits, given the observed changes in unit cell volume of the phases within the two phase region.

The changes of the a, b, and c lattice parameters with composition for each phase are given in Fig. 9, with three separate regions to consider. There are several effects occurring that influence the volume of the unit cell. The changes in the lattice parameter may be explained in terms of the structure distorting to accommodate the ionic size and coordination preference differences between Mn^{4+}, Mn^{3+}, and Fe^{3+}. For example, a volume decrease occurs with the substitution of the smaller Mn^{4+} for the Fe^{3+}.

The edge-sharing octahedra in the structure provide a limitation to the ways in which the octahedra can distort in the $Bi_2Mn_4O_{10}$ and $Bi_2Fe_4O_9$ structures. The distortion may be quantified using the octahedral distortion parameter, Δd, and is calculated using the following equation [33]:

$$\Delta d = \frac{1}{6} \sum_{n=1,6} \left[\frac{[d_n - (d)]}{(d)} \right]^2$$

where (d) is the mean M–O distance and d_n are the individual M–O bond distances. The octahedral distortion values, $\Delta d(\times 10^4)$,

Table 1
Fitted hyperfine parameters, area fractions, and iron cation fractions on different sites in $Bi_2Fe_{4-x}Mn_xO_{10-\delta}$ solid solutions assuming two different sites in the $Bi_2Fe_{4-x}Mn_xO_9$ phases.

x_{Mn}	Species	IS (mm/s)	QS (mm/s)	σ_{QS} (mm/s)	$\Gamma/2$ (mm/s)	Area (%)	Iron cation fraction (%)
0	Fe^{3+} (octa)	0.346 (2)	0.365 (3)	0.042 (19)	0.114 (4)	49.75 (37)	50
	Fe^{3+} (tetra)	0.226 (1)	0.936 (3)	0.035 (23)	0.114 (4)	50.25 (46)	50
0.25	Fe^{3+} (octa)	0.345 (2)	0.375 (3)	0.0045 (23)	0.117 (5)	46.74 (52)	46.78
	Fe^{3+} (tetra)	0.234 (2)	0.941 (3)	0.0083 (14)	0.117 (5)	53.26 (52)	53.21
0.5	Fe^{3+} (octa)	0.343 (2)	0.389 (4)	0.043 (28)	0.126 (5)	43.18 (53)	43.23
	Fe^{3+} (tetra)	0.242 (2)	0.950 (3)	0.1140 (13)	0.126 (5)	56.82 (53)	56.77
0.75	Fe^{3+} (octa)	0.343 (1)	0.394 (2)	0.079 (9)	0.115 (3)	41.31 (29)	41.36
	Fe^{3+} (tetra)	0.245 (1)	0.955 (2)	0.1472 (62)	0.115 (3)	58.69 (29)	58.64
0.875	Fe^{3+} (octa)	0.340 (2)	0.418 (4)	0.081 (18)	0.121 (6)	39.03 (60)	39.08
	Fe^{3+} (tetra)	0.245 (2)	0.956 (4)	0.158 (12)	0.121 (6)	60.97 (60)	60.92
3	Fe^{3+} (octa)	0.315 (4)	0.714 (30)	0.159 (29)	0.115 (3)	29.2 (29)	19.24
	Fe^{3+} (pyr)	0.315 (4)	1.118 (8)	0.1	0.115 (3)	70.8 (29)	70.76
3.125	Fe^{3+} (octa)	0.314 (5)	0.748 (75)	0.214 (49)	0.113 (6)	31.2 (68)	31.24
	Fe^{3+} (pyr)	0.295 (2)	1.121 (9)	0.087 (17)	0.113 (6)	69.8 (61)	68.76
3.25	Fe^{3+} (octa)	0.315 (3)	0.645 (15)	0.12	0.126 (4)	28.2 (11)	28.24
	Fe^{3+} (pyr)	0.305 (1)	1.103 (4)	0.974 (16)	0.126 (4)	71.8 (11)	68.76
3.5	Fe^{3+} (octa)	0.305	0.706	0.324 (63)	0.112 (11)	22.0 (26)	22.03
	Fe^{3+} (pyr)	0.301 (2)	1.113 (7)	0.046 (44)	0.112 (11)	78.0 (26)	77.97
3.75	Fe^{3+} (octa)	0.306 (56)	0.668	0.32 (11)	0.122 (11)	10.2 (29)	10.22
	Fe^{3+} (pyr)	0.306 (3)	1.136	0 (1.2)	0.122 (11)	89.8 (29)	89.78
3.875	Fe^{3+} (octa)	0.291 (45)	0.72 (27)	0.35	0.130 (15)	8.1 (24)	8.11
	Fe^{3+} (pyr)	0.306 (3)	1.131 (17)	0.09 (38)	0.130 (15)	91.9 (24)	91.89

Fig. 6. ^{57}Fe-Mössbauer room temperature spectra of selected $Bi_2Fe_{4-x}Mn_xO_{10}$ samples, $x=3$, 3.5, and 3.875. The blue lines represented the doublet assigned to octahedrally coordinated Fe^{3+}, and the green lines represented the doublet assigned to tetragonal-pyramidally coordinated Fe^{3+}. (For interpretation of the references to color in this figure legend, the reader is referred to the web version of this article.)

Fig. 7. Fraction of iron cations on site types versus manganese content x in $Bi_2Fe_{4-x}Mn_xO_{10-\delta}$. O, T, and P indicated octahedrally, tetrahedrally, and pyramidally coordinated sites. In the upper graph, the Mössbauer spectra of the $Bi_2Fe_4O_9$- and $Bi_2Mn_4O_{10}$-type samples have been evaluated with a two-site model assuming O (blue squares) and T (red circles) or P (green triangles) sites. In the lower graph, a three-site model has been employed for the $Bi_2Fe_4O_9$-type samples with O (blue squares), T (red circles), and P (green triangles) sites. Open symbols refer to the work of Nguyen et al. [28]. (For interpretation of the references to color in this figure legend, the reader is referred to the web version of this article.)

are 0.441 and 0.522 for $Bi_2Mn_4O_{10}$ and $Bi_2Fe_4O_9$, respectively [12,15]. These distortion values are large relative to structures with fewer geometrical restrictions, e.g. 0.003 for $CaMnO_3$ [34], 0.028 for $SrMnO_3$ [35], and 0.002 for $LaFeO_3$ [36], all of which are perovskite related structures containing corner-sharing octahedra. The octahedra in the $Bi_2M_4O_{10/9}$ series are already distorted and limited in further distortions as other cations are introduced. A limit is reached in which the structure is less stable than a secondary phase that is formed.

In $Bi_2Mn_4O_{10}$ the Mn^{3+} has been assigned to the tetragonal pyramidal sites and Mn^{4+} to the octahedral sites [15]. A bond valence sum (BVS) analysis of the $Bi_2Mn_4O_{10}$ structure supports this assignment, with a calculated BVS of 3.05 v.u. for Mn^{3+} on the tetragonal pyramidal site and 3.88 v.u. for Mn^{4+} on the octahedral site. The reported crystal structures of $Bi_2Fe_4O_9$ exhibit a larger deviation, with calculated BVS of 2.88 v.u. for Fe^{3+} on the tetrahedral site and 3.31 v.u. for Fe^{3+} on the octahedral site [12,23]. In related phases containing both Fe and Mn in this structure type, the distribution of cations and degree of ordering varies. The structure of $Bi_2Fe_2Mn_2O_{10}$ grown as a single crystal from a flux was reported to have ordered Fe^{3+} and Mn^{4+} on the octahedral and tetragonal pyramidal sites, respectively, on the basis of single crystal XRD [27]. For comparison, the structures of $Y_2Fe_2Mn_2O_{10}$ and $Yb_2Fe_2Mn_2O_{10}$ synthesized under high O_2 pressure were reported to have mostly or completely ordered Fe^{3+} and Mn^{4+} on the square pyramidal and octahedral sites, respectively [37–39]. A bond valence sums analysis of $Bi_2Fe_2Mn_2O_{10}$ supports

site assignments, Mn^{4+} primarily octahedral and Fe^{3+} primarily tetragonal pyramidal, as was reported for $Y_2Fe_2Mn_2O_{10}$ and $Yb_2Fe_2Mn_2O_{10}$.

In the iron substituted $Bi_2Mn_4O_{10}$-type, the distribution of transition metal cations between octahedral and tetragonal pyramidal sites was previously studied using X-ray powder diffraction, ^{57}Fe Mössbauer spectroscopy, and magnetic measurements [28]. Nguyen et al. reported a mixed site occupancy, with Fe^{3+} and Mn^{3+} showing preference for tetragonal pyramidal sites and Mn^{4+} preference for octahedral sites in the $Bi_2Mn_4O_{10}$ structure model for $Bi_2Mn_3FeO_{10}$, which indicated a mixed site occupancy with a complex cation distribution presented as $Bi_2[Mn_{1.66}^{4+}Fe_{0.34}^{3+}]_{oct}$ $[Mn_{1.00}^{3+}Mn_{0.34}^{4+}Fe_{0.66}^{3+}]_{tet.pyd.}O_{10}$ for one composition.

The high-spin six-coordinate ionic radius is 0.645 Å for both Fe^{3+} and Mn^{3+} and 0.530 Å for Mn^{4+} [40]. The transition metal cations may occupy one or two of two possible Wyckoff sites in both the $Bi_2Mn_4O_{10}$-type and $Bi_2Fe_4O_9$-type structure. A change in cation distribution can be used to clarify the observations of changes in the Mössbauer spectra and results from X-ray diffraction. The change in volume with composition is related to the
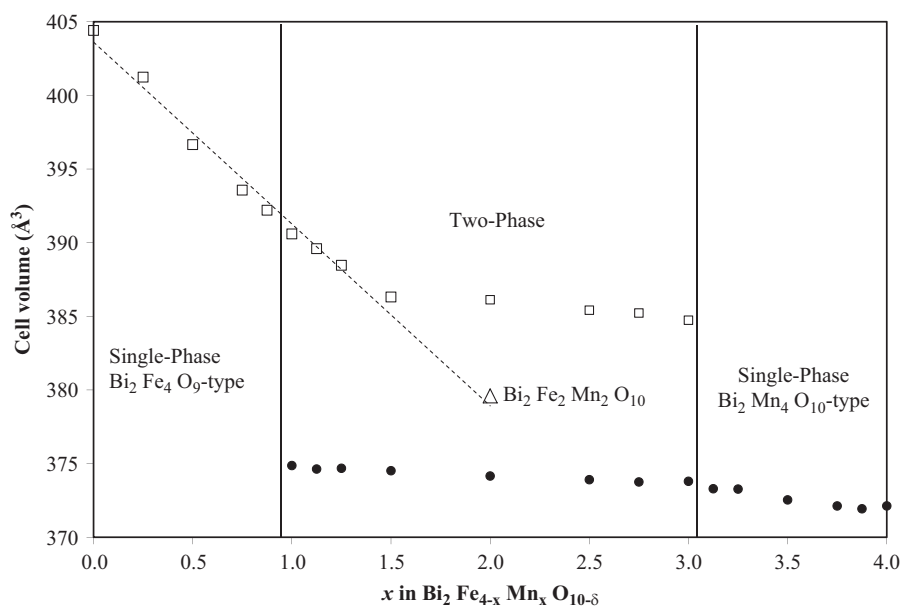
Fig. 8. Unit cell volume as a function of composition (x) in $Bi_2Fe_{4-x}Mn_xO_{10-\delta}$ for samples heated to 825 °C. Open squares represent a phase related to $Bi_2Fe_4O_9$-type and full circles to $Bi_2Mn_4O_{10}$-type. The triangle represents the single-crystal $Bi_2Fe_2Mn_2O_{10}$. Vertical guide lines separate single phase and two phase regions and the dashed line is a guide to the eye.
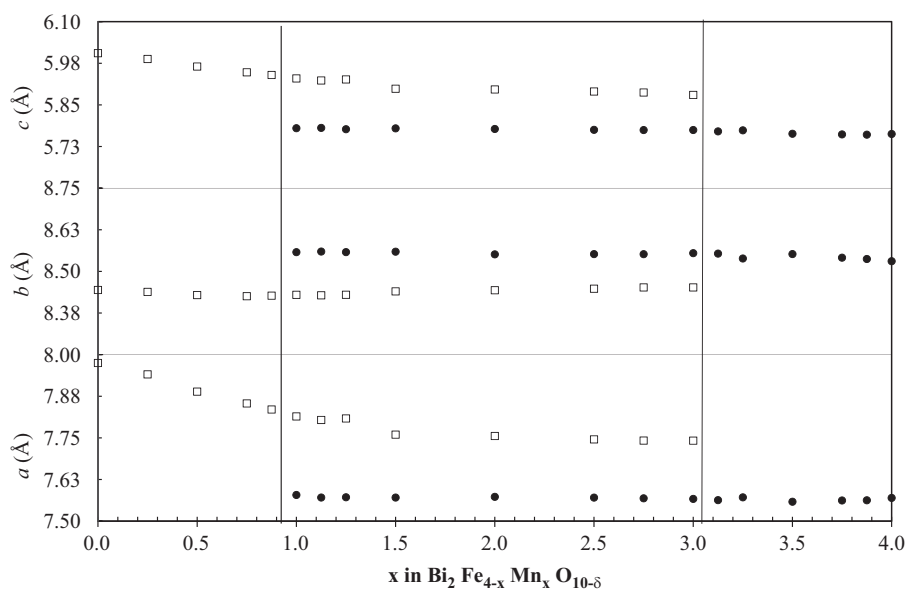
Fig. 9. Lattice parameters as a function of composition (x) in $Bi_2Fe_{4-x}Mn_xO_{10-\delta}$ for samples annealed at 825 °C. Open squares represent a phase related to $Bi_2Fe_4O_9$-type and filled circles $Bi_2Mn_4O_{10}$-type. Vertical guide lines separate single- and two-phase regions.

differences in size and coordination environment preferences of transition metal cations. Clearly the transition metal cation site distributions and oxidation states are complex, even for the single-phase samples in the solid solution region. In the following subsections, each of the three regions is discussed in more detail.

4.2. Single-phase $Bi_2Mn_4O_{10}$-type

The Mössbauer parameters very clearly reflect the significant changes at the two structural cation sites in the $Bi_2M_4O_9$ and in the $Bi_2M_4O_{10}$ structure: the quadrupolar splitting at the octahedrally coordinated sites is changing from about 0.4 mm/s in the $Bi_2M_4O_9$ structure to 0.7 mm/s in the $Bi_2M_4O_{10}$ structure. Similarly, the quadrupolar interactions at the non-octahedral sites change. For the non-octahedral (i.e. tetrahedral and possibly

tetragonal pyramidal) site in the $Bi_2M_4O_9$ structure, the splitting takes a value of about 0.9 mm/s whereas 1.1 mm/s are observed for the tetragonal pyramidal site in the $Bi_2M_4O_{10}$ structure, see Tables 1 and 2. Thus, both structural sites are more strongly distorted in the $Bi_2M_4O_{10}$ structure. There is no conflict with the distortion parameter because different distortions are involved with the quadrupolar interaction reflecting asymmetric charge distribution in the lattice sites around the Fe^{3+}. Also the isomer shifts of iron are influenced by the structural changes. The value for the tetrahedral site in $Bi_2M_4O_9$-type of about 0.24 mm/s compares with an isomer shift of about 0.30 mm/s for the pyramidal site which is evidence of the increased coordination number of the latter site in the $Bi_2M_4O_{10}$ phase. These findings from Mössbauer spectroscopy are in perfect agreement with the considerations of composition dependent structural parameters

Table 2
Hyperfine parameter and area of $Bi_3Fe_{4-x}Mn_xO_{9+\delta}$ and $Bi_3Fe_{4-x}Mn_xO_{10-\delta}$ samples assuming three different sites in the of $Bi_3Fe_{4-x}Mn_xO_{9+\delta}$ phases.

x_{Mn}	Species	IS	QS	σ_{QS}	$\Gamma/2$	Area (%)	Iron cation fraction (%)
0	Fe^{3+} (octa)	0.346 (2)	0.365 (3)	0.042 (19)	0.114 (4)	49.95 (46)	50.00
	Fe^{3+} (tetra)	0.226 (1)	0.936 (3)	0.035 (23)	0.114 (4)	50.05 (46)	50.00
0.25	Fe^{3+} (octa)	0.345 (2)	0.375 (5)	0.082 (21)	0.106 (9)	47.3 (60)	47.30
	Fe^{3+} (tetra)	0.231 (9)	0.934 (10)	0.082 (21)	0.106 (9)	47 (6)	46.91
	Fe^{3+} (pyr)	0.304 (55)	1.12 (26)	0.16 (17)	0.106 (9)	5.7 (85)	5.79
0.5	Fe^{3+} (octa)	0.343 (2)	0.391 (4)	0.078 (17)	0.119 (5)	44.1 (23)	44.19
	Fe^{3+} (tetra)	0.239 (3)	0.928 (10)	0.1	0.119 (5)	48.2 (26)	48.21
	Fe^{3+} (pyr)	0.287 (17)	1.17 (5)	0.03 (9)	0.119 (5)	7.7 (31)	7.60
0.75	Fe^{3+} (octa)	0.343 (1)	0.397 (2)	0.073 (10)	0.107 (4)	42.5 (16)	42.55
	Fe^{3+} (tetra)	0.242 (2)	0.935 (10)	0.139 (13)	0.107 (4)	50.6 (18)	50.56
	Fe^{3+} (pyr)	0.301 (22)	1.190 (29)	0.088 (44)	0.107 (4)	6.9 (2.3)	6.89
0.875	Fe^{3+} (octa)	0.340 (2)	0.421 (5)	0.109 (17)	0.112 (7)	40.3 (14)	40.35
	Fe^{3+} (tetra)	0.249 (2)	0.945 (10)	0.155 (18)	0.112 (7)	55.3 (17)	55.26
	Fe^{3+} (pyr)	0.322 (33)	1.255 (43)	0.040 (16)	0.112 (7)	4.4 (17)	4.40
3	Fe^{3+} (octa)	0.315 (4)	0.714 (30)	0.159 (29)	0.115 (3)	29.2 (29)	29.24
	Fe^{3+} (pyr)	0.315 (4)	1.118 (8)	0.1	0.115 (3)	70.8 (29)	70.76
3.125	Fe^{3+} (octa)	0.314 (5)	0.748 (75)	0.214 (49)	0.113 (6)	31.2 (68)	31.24
	Fe^{3+} (pyr)	0.395 (2)	1.121 (9)	0.087 (17)	0.113 (6)	69.8 (61)	68.76
3.25	Fe^{3+} (octa)	0.315 (3)	0.645 (15)	0.12	0.126 (4)	28.2 (11)	28.24
	Fe^{3+} (pyr)	0.305 (1)	1.103 (4)	0.074 (16)	0.126 (4)	71.8 (11)	71.76
3.5	Fe^{3+} (octa)	0.305	0.706	0.324 (63)	0.112 (11)	22.0 (26)	22.03
	Fe^{3+} (pyr)	0.301 (2)	1.113(7)	0.046 (44)	0.112 (11)	78.0 (26)	77.97
3.75	Fe^{3+} (octa)	0.306 (56)	0.668	0.32 (11)	0.122 (11)	10.2 (29)	10.22
	Fe^{3+} (pyr)	0.306 (3)	1.136	0 (1.2)	0.122 (11)	89.8 (29)	89.78
3.875	Fe^{3+} (octa)	0.291 (45)	0.72 (27)	0.35	0.130 (15)	8.1 (24)	8.11
	Fe^{3+} (pyr)	0.306 (3)	1.131 (17)	0.09 (38)	0.130 (15)	91.9 (24)	91.89

derived from X-ray diffraction and are also in agreement with results for the structurally related $YFeMnO_5$ ($Y_2Fe_2Mn_2O_{10}$) [37,38], where iron almost exclusively occupies the square pyramidal position.

In contrast to the large volume change of the $Bi_2Fe_4O_9$-type phase (-3.11%, see below), the volume change for the single-phase $Bi_2Mn_4O_{10}$-structured ($3 < x < 4$) phase is smaller at 1.48 $Å^3$ ($+0.40\%$) over the solid solution range and is attributed primarily to substitution of Fe^{3+} for the similarly sized Mn^{3+} on the tetragonal pyramidal site. A slight volume increase was also observed in $Yb(Mn_{1-x}Fe_x)O_3$ samples as Fe^{3+} replaced Mn^{3+} in the five-coordinate sites.[41] The lattice parameters show minimal change as the Fe:Mn ratio changes, with a, b, and c increasing length by 0.0017 Å (0.02%), 0.0160 Å (0.19%), and 0.0118 Å (0.20%), respectively. We attribute the Fe substitution into the $Bi_2Mn_4O_{10}$-type structure to occur via substitution onto both the octahedral and tetragonal pyramidal sites, with a preference for occupation on the tetragonal pyramidal site, while still maintaining primarily the $Bi_2Mn_4O_{10}$-type structure. As mentioned earlier, the ionic radii of Mn^{3+} and Fe^{3+} are similar and substitution on the tetragonal pyramid site is expected to exhibit minimal change in the unit cell volume and lattice parameters. These data suggest a minimal deviation from full oxygen stoichiometry in the $Bi_2M_4O_{10}$ composition, as was previously indicated in the mixed site distribution and stoichiometric oxygen assignment by Nguyen et al. [28].

4.3. Single-phase $Bi_2Fe_4O_9$-type

The cell volumes and lattice parameters from X-ray diffraction in Figs. 8 and 9 show the solid solution regions near the end members approximately follow Vegard's law. A relatively large change in unit cell volume is evident as Mn is substituted into the $Bi_2Fe_4O_9$ structure type. The change in unit cell volume for the single-phase $Bi_2Fe_4O_9$-type compound ($0 < x < 0.875$) is 11.2 $Å^3$ (-3.11%). The lattice parameters of the $Bi_2Fe_4O_9$-structured phase ($0 < x < 0.875$) decrease with increasing x with a, b, and c decreasing lengths by 0.134 Å (-1.71%), 0.0204 Å (-0.24%), and 0.0579 Å (-0.96%), respectively. The a lattice parameter of the $Bi_2Fe_4O_9$-structured phase is large (7.976 Å) compared to the a of the $Bi_2Mn_4O_{10}$ phase (7.569 Å), which is primarily related to the differences between the tetrahedra and tetragonal pyramids of the two end member structures. The significant decrease of the unit cell volume with increasing Mn content, shown with a linear fit to the unit cell volume versus composition ($0 < x < 1.5$) and is forecasted to $x=2$ in Fig. 8, shows a trend towards the reported cell volume for a $Bi_2Fe_2Mn_2O_{10}$ single crystal, indicating the possibility that the smaller and more symmetric Mn^{4+} may play a role. This ion would possess a natural selectivity for the octahedral site with the higher coordination number.

Two models were investigated in the analysis of the Mössbauer data (Fig. 5a, b, and 6), (i) Fe^{3+} in octahedral and tetrahedral sites, and (ii) Fe^{3+} in octahedral, tetrahedral, and pyramidal sites. The fits to Mössbauer data were excellent using both models and indicate a preference of Mn for the six-fold coordinated sites, but do not indicate the oxidation state of Mn, which is expected to adopt a tetravalent and/or trivalent state.

There are several possible mechanisms for the introduction of Mn in place of Fe^{3+} into the $Bi_2M_4O_9$ structure, including: (i) the formation of vacancies on Bi- and/or on M-sites, for charge compensation upon Mn^{4+} substitution at the octahedral site, (ii) Mn^{4+} substitution at the octahedral site with incorporation of additional oxygen for charge compensation in the 4e ($0,0,z\sim0.29$) pyramidal site, occurring in place of the O at the tetrahedral 2b site (0,0,1/2), and/or (iii) substitution of Mn^{3+} for Fe^{3+} on the octahedral site.

Considering the bismuth vacancy mechanism for the sample $x=0.875$, if Mn^{4+} is taken to fully occupy the octahedral site and
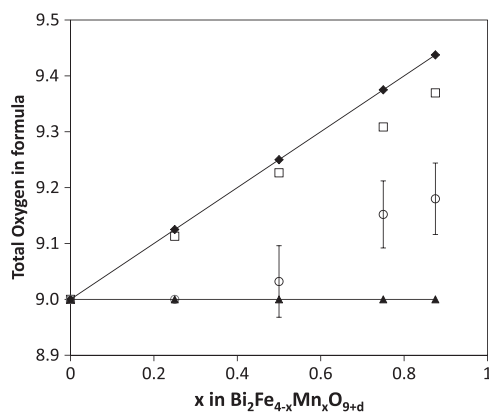
Fig. 10. Total oxygen content versus composition for $0 < x < 1$. Diamonds represent oxygen content based on formula $Bi_2Fe_{4-x}Mn_xO_{9+x/2}$, squares are from a three-site Mössbauer analysis, circles are from X-ray diffraction, and triangles represent substitution of Mn^{3+} for Fe^{3+}.

the charge balance was obtained by bismuth vacancies, the resulting chemical formula may be written as $Bi_{2-x/3}[Fe_{2-x} Mn_x]_{(oct)}[Fe_2]_{(tet)}O_9$. Refinements of the bismuth occupancy increased towards the ideal full occupancy even for the $x = 0.875$ sample, and if the occupancy was fixed according to the idealized formula, the isotropic thermal parameters increased to unrealistically large values. Analogous results were found when investigating vacancies on the transition metal sites. In the course of studying the Bi–Mn–Fe–O phase equilibria, these mullite-type structured phases do not appear to tolerate bismuth deficiency and show Fe_2O_3 or Mn_2O_3 secondary phases when prepared according to the formula given above [42]. These results indicate Bi- or M-vacancy compensation mechanism is not the primary site substitution mechanism, however partial cation vacancy formation cannot be ruled out solely based on these data.

The incorporation of additional O into the structure is a second possible substitution and charge compensation mechanism. The idealized chemical formula, assuming all Mn^{4+} and Fe^{3+}, may be written as $Bi_2[Fe_{2-x}]_{tet}[Fe_x]_{pyr}[Fe_{2-x}Mn_x]_{oct}O_{9+x/2}$ for $0 < x < 1$. As Mn is substituted in place of Fe, in accordance with Mössbauer data, it primarily occupies the octahedral site. In order to maintain charge balance in this structure model, additional oxygen is incorporated onto the O1 on the 4e site, to give $[FeO_5]$ tetragonal pyramids (Fig. 1b), in place of O1 site occupancy on the 2b site (Fig. 1a) that gives $[FeO_4]$ tetrahedra. In this model, the Fe that primarily occupies the non-octahedral 4h site is coordinated to either the oxygen that occupies the 2b site to form tetrahedra, or the O that occupies the 4e site to form $[FeO_5]$ tetragonal pyramids, with incomplete occupancy for each of the two sites for $x > 0$. Iron is known to occupy both types of coordination environments in the tetrahedral site in $Bi_2Fe_4O_9$ and a tetragonal pyramidal site in $Y_2Fe_2Mn_2O_{10}$, $Yb_2Fe_2Mn_2O_{10}$, and $Bi_2Fe_2Mn_2O_{10}$ [27,37,39].

A third possible mechanism is the substitution of Mn^{3+} for Fe^{3+} on the octahedral sites, which would enable the structure to maintain the stoichiometric $Bi_2M_4O_9$-type. Despite the differences in coordination preferences between the symmetric Fe^{3+} and Jahn-Teller Mn^{3+}, the ions are known to fully substitute in octahedral coordination in a variety of compounds, one being the perovskite series $LaFe_{1-x}Mn_xO_3$. Although the ionic radii are similar, a significant volume decrease is observed in intermediate compounds. The unit cell volumes of $LaFeO_3$ [36], $La(Fe_{0.5} Mn_{0.5})O_3$ [43], and $LaMnO_3$ [44] are 243.02 Å^3, 237.56 Å^3, and 244.80 Å^3, respectively. The 3.04% decrease in unit cell volume of the intermediate composition is of the same order as the 3.11% unit cell volume decrease as observed from $Bi_2Fe_4O_9$ at the $x = 0.875$ solid solution limit. The discrepancy in the refined site

occupancies suggests the direct substitution of Mn^{3+} for Fe^{3+} on the octahedral sites is also a plausible substitution mechanism and may simultaneously occur along with Mn^{4+} substitution.

The total oxygen content (i.e. $O_{9+\delta}$) versus composition is shown in Fig. 10. The model 3, substituting Mn^{3+} for Fe^{3+}, results in oxygen content of 'O_9' throughout the series is shown by triangles. The oxygen content for complete Mn^{4+} on octahedral sites and no cation vacancies (substitution model 2, $Bi_2[Fe_{2-x}]_{tet} [Fe_x]_{pyr}[Fe_{2-x}Mn_x]_{oct}O_{9+x/2}$) is presented as diamonds. A constrained refinement (occ. of O(2b)+occ. O(4e)=1) of the site occupancies for the oxygen atoms on the 2b and 4e sites was performed. If the site refined to full occupancy, it was fixed at the full value. The total oxygen content from refinements of X-ray diffraction data are presented as circles. Additionally, the total oxygen content using values from the three-site Mössbauer fit, Fig. 7 bottom, is shown as squares and obtained by using the chemical composition and iron cation fraction on each of the three sites, assuming all Mn^{4+} to complete the occupancy of the octahedral site and the remaining Mn shares the pyramidal site with Fe. Both the X-ray diffraction and Mössbauer data suggest lower oxygen content than predicted using all Mn^{4+}, but with a higher value than expected for all Mn^{3+}. It should be noted that although XRD is somewhat insensitive to oxygen content, refinements of the $Bi_2Fe_4O_9$-type phases improved with refinements using two oxygen sites, whereas the $Bi_2Mn_4O_{10}$-type phase did not show any indication for oxygen at the tetrahedral 2b Wyckoff site (see Supplemental Information).

The coordination flexibility and site disorder of the transition metal ions enable the structure to compromise in the optimization of the edge-sharing octahedra, which connect to the edge of the tetrahedra or the base of the tetragonal pyramid. Given the results of the X-ray diffraction and Mössbauer experiments, site substitution appears to occur primarily by replacement of manganese for Fe^{3+} on the octahedral site and it appears likely that more than one type of substitution mechanism contributes. Our interpretations of these data suggest not all the Mn is incorporated as Mn^{4+} on the octahedral site, as was found for $Bi_2Mn_2Fe_2O_{10}$, but the possibility for both (i) Mn^{4+} substitution on the octahedral site and formation of Fe^{3+} tetragonal pyramids and (ii) direct substitution of Mn^{3+} for Fe^{3+} on the octahedral site. Further studies, e.g. single crystal, neutron diffraction, PDF analysis, spectroscopic techniques and/or oxygen fugacity synthesis experiments are needed to further clarify the substitution mechanism(s) in these materials, but those studies are beyond the scope of the current contribution.

4.4. Two-phase mixed $Bi_2Fe_4O_9$-type and $Bi_2Mn_4O_{10}$-type

The two phases in the intermediate region have substantially different unit cell volumes and indicate the two phases primarily retain the structures related to the end members. There is a relatively smaller change, 1.1 Å^3 (0.29%), in the volume for the $Bi_2Mn_4O_{10}$-type phase, whereas a larger change, 6.0 Å^3 (1.5%), is found for the $Bi_2Fe_4O_9$-type compound. In the two-phase region, the unit cell volume of the $Bi_2Mn_4O_{10}$-type structure exhibits only minimal change, whereas the change in volume of the $Bi_2Fe_4O_9$-type phase suggests the composition of the phase is also changing, rather than merely a change of the relative amounts of the solid solution end members at $x \approx 1$ and 3. Interestingly, the volume change of the $Bi_2Fe_4O_9$-type phase changes more rapidly from $x = 1.0$ to 1.5 than from $x = 1.5$ to 2.875. At $x = 1$, half of the octahedral Fe has been replaced with Mn. Between $1 < x < 1.5$, we suggest that the substitution of Mn continues primarily at the octahedral site. The change in unit cell volume may indicate a change in site and/or oxidation state substitution. Under strongly oxidizing condition of high O_2 pressure for $A_2Fe_2Mn_2O_{10}$ ($A=Y$, Yb)

or in bismuth oxide flux for $Bi_2Fe_2Mn_2O_{10}$, continued substitution occurs until the structure is composed of only octahedral Mn^{4+} and tetragonal pyramidal Fe^{3+} at $x=2$. The $Bi_2M_4O_9$-type phase forms in equilibrium with a $Bi_2M_4O_{10}$-type phase with approximate composition of the solid solution limit near $Bi_2FeMn_3O_{10}$. There are two trends in the amount of each phase throughout the series (Fig. 4), between $1 < x < 1.5$ only a slight change in amount is observed, whereas near 1.5 the amount of the secondary phase begins to rapidly increases with additional substitution. Given the smaller volume changes of the two phases in $1.5 < x < 3$, we attribute this to a change in the amounts of the phases as the primary change and a minor change in the chemical composition of each of the two phases.

It is interesting that flux-derived single crystals in the $Bi_2Fe_4O_9$–$Bi_2Mn_4O_{10}$ system with $Bi_2Fe_2Mn_2O_{10}$ composition were described by Giaquinta and zur Loye [27]. The question remains why in powder syntheses a large miscibility gap does occur while for single crystals the gap is much smaller. Since we believe that our powder synthesis technique produced phases being in the thermodynamic equilibrium in air, the single crystals may be not. Problems will be discussed in more detail in a coming article dealing with single crystal studies in the $Bi_2Fe_4O_9$–$Bi_2Mn_4O_{10}$ composition range.

5. Conclusions

Our investigation of the cation substitution in the $Bi_2Fe_4O_9$–$Bi_2Mn_4O_{10}$ composition range yielded limited mixed crystal formation near to the end members at 825 °C, although both structures are closely related. Only slightly extended mixed crystal regions can be expected by increasing the synthesis temperature just below the stability limit (approx. 850 °C). A solid solution region is found near each end member with a two-phase region at intermediate compositions. The mixed crystal limits agree with those of the previous report by Masuno [25] of a partial solid solution $Bi_2Fe_{4-x}Mn_xO_{10-\delta}$ at the Fe-rich side with $0 \le x < \approx 0.9$, but differ for the Mn-rich side, which was given by Masuno with $3.6 \le x \le 4$. Our results are in close agreement with Nguyen et al. that described a solid solution extending from $3 \le x \le 4$ for the $Bi_2Mn_4O_{10}$-related phase [28].

In the $Bi_2Fe_4O_9$-related structure a relatively strong decrease of the unit cell volume is observed. This is interpreted in terms that most of the Mn does substitute Fe^{3+} primarily in the octahedra as Mn^{4+} and a smaller fraction as Mn^{3+}, both of which tend to decrease the unit cell volume. Charge compensation then may be effected by addition of O and local formation of fivefold coordinated $[FeO_5]$ tetragonal pyramids. This means that at least under highly oxidizing environments a complete solid solution range between the $Bi_2Fe_4O_9$-related structure and $Bi_2Fe_2Mn_2O_{10}$ with a $Bi_2Mn_4O_{10}$-related structure may exist. In the $Bi_2Mn_4O_{10}$-related structure a relatively small change of the unit cell volume occurs with increasing Fe^{3+} incorporation. This is attributed to substitution of similarly sized Mn^{3+} by Fe^{3+} at the pyramidal lattice site.

We believe that the powder data represent stable phase relationships in the $Bi_2Fe_4O_9$–$Bi_2Mn_4O_{10}$ mixed crystal system with a relatively wide miscibility gap between the $Bi_2Fe_4O_9$- and the $Bi_2Mn_4O_{10}$-related phases. On the contrary the single crystals, e.g. described by Giaquinta and zur Loye [27] with a composition $Bi_2Fe_2Mn_2O_{10}$ may form metastably.

Appendix A. Supporting information

Supplementary data associated with this article can be found in the online version at doi:10.1016/j.jssc.2011.10.046.

References

[1] I. Bloom, M.C. Hash, J.P. Zebrowski, K.M. Myles, M. Krumpelt, Solid State Ionics 739 (1992) 53–56.
[2] I. Abrahams, A.J. Bush, G.E. Hawkes, T. Nunes, J. Solid State Chem. 147 (1999) 631.
[3] A.S. Poghossian, H.V. Abovian, P.B. Avakian, S.H. Mkrtchian, V.M. Haroutunian, Sens. Actuators B 4 (1991) 545.
[4] J.B. Goodenough, A. Manthiram, P. Paranthaman, Y.S. Zhen, Solid State Ionics 52 (1992) 105.
[5] N.I. Zakharchenko, Kinet. Catal. 43 (2002) 95.
[6] Q.- Ruan, W.- Zhang, J. Phys. Chem. C 113 (2009) 4168.
[7] S. Sun, W. Wang, L. Zhang, M. Shang, J. Phys. Chem. B 113 (2009) 12826.
[8] A.K. Singh, S.D. Kaushik, B. Kumar, P.K. Mishra, A. Venimadhav, V. Siruguri, S. Patnaik, Appl. Phys. Lett. 92 (2008) 132910.
[9] A.F. Garcia-Flores, E. Granado, H. Martinho, R.R. Urbano, C. Rettori, E.I. Golovenchits, V.A. Sanina, S.B. Oseroff, S. Park, S.- Cheong, Phys. Rev. B 73 (2006) 104411.
[10] N.A. Hill, J. Phys. Chem. B 104 (2000) 6694.
[11] A.G. Tutov, V.N. Markin, Izv. Akad. Nauk SSSR, Neorg. Mater. 6 (1970) 2014.
[12] N. Niizeki, M. Wachi, Z. Kristaogr. Kristallgeom. Kristallphys. Kristalchem. 127 (1968) 173.
[13] N. Shamir, E. Gurewitz, Acta Cryst. A A34 (1978) 662.
[14] E.F. Bertaut, G. Buisson, S. Quezel-Amrunaz, G. Quezel, Solid State Commun. 5 (1967) 25.
[15] A. Munoz, J.A. Alonso, M.T. Casais, M.J. Martinez-Lope, J.L. Martinez, M.T. Fernandez-Diaz, Phys. Rev. B 65 (2002) 144423.
[16] H. Schneider, J. Schreuer, B. Hildmann, J. Eur. Ceram. Soc. 28 (2008) 329.
[17] T. Debnath, C.H. Rüscher, P. Fielitz, S. Ohmann, G. Borchardt, J. Solid State Chem. 183 (2010) 2582.
[18] S. Zha, J. Cheng, Y. Liu, X. Liu, G. Meng, Solid State Ionics 156 (2003) 197.
[19] Y.J. Wu, N. Wang, Y.Q. Lin, X.Q. Liu, X.M. Chen, Mater. Chem. Phys. 121 (2010) 326.
[20] Z.H. Sun, B.L. Cheng, S. Dai, K.J. Jin, Y.L. Zhou, H.B. Lu, Z.H. Chen, G.Z. Yang, J. Appl. Phys. 99 (2006) 084105.
[21] D.M. Giaquinta, G.C. Papaefthymiou, W.M. Davis, H.- Zur Loye, J. Solid State Chem. 99 (1992) 120.
[22] D.K. Shukla, S. Mollah, R. Kumar, P. Thakur, K.H. Chae, W.K. Choi, A. Banerjee, J. Appl. Phys. 104 (2008) 033707.
[23] Y. Du, Z.X. Cheng, S.X. Dou, X.L. Wang, Mater. Lett. 64 (2010) 2251.
[24] K.L. Da Silva, V. Scaronepelák, A.P. Jr., F.J. Litterst, K. Becker, Z. Anorg. Allg. Chem. 636 (2010) 1018.
[25] K. Masuno, Nippon Kagaku Zasshi 88 (1967) 726.
[26] C. Moure Jimenez, Bol. Soc. Esp. Ceram. V (1978) 365.
[27] D.M. Giaquinta, H.-C. zur Loye, J. Alloys Compd. 184 (1992) 151.
[28] N. Nguyen, M. Legrain, A. Ducouret, B. Raveau, J. Mater. Chem. 9 (1999) 731.
[29] G. Huo, Z. Gu, M. Qiu, J. Alloys Compd. 381 (2004) 317.
[30] J. Rodriguez-Carvajal, FULLPROF: A Program for Rietveld Refinement and Pattern Matching Analysis, 1990.
[31] K. Lagarec, D.G. Rancourt, Recoil-Mössbauer Spectra Analysis Software for Windows, 1998, 1.02.
[32] D.M. Giaquinta, G.C. Papaefthymiou, H.-C. zur Loye, J. Solid State Chem. 114 (1995) 199.
[33] J.A. Alonso, M.J. Martinez-Lope, M.T. Casais, M.T. Fernandez-Diaz, Inorg. Chem. 39 (2000) 917.
[34] K.R. Poeppelmeier, M.E. Leonowicz, J.C. Scanlon, J.M. Longo, J. Solid State Chem. 45 (1982) 71.
[35] K. Kuroda, N. Ishizawa, N. Mizutani, M. Kato, J. Solid State Chem. 38 (1981) 297.
[36] M. Marezio, J.P. Remeika, P.D. Dernier, Acta Cryst. B B26 (1970) 2008.
[37] A. Munoz, J.A. Alonso, M.J. Martinez-Lope, J.L. Martinez, Chem. Mater. 21 (2004) 4087.
[38] F. Wunderlich, T. Leisegang, T. Weisbach, et al., Phys. Rev. B 82 (2010) 014409.
[39] M.J. Martínez-Lope, M. Retuerto, J.A. Alonso, M. García-Hernández, K. Krezhov, I. Spirov, T. Ruskov, M.T. Fernández-Díaz, Solid State Commun. 149 (2009) 540.
[40] R.D. Shannon, Acta Cryst. A 32 (1976) 751.
[41] Y. Huang, M. Karppinen, N. Imamura, H. Yamauchi, J.B. Goodenough, Phys. Rev. B 76 (2007) 174405.
[42] M.W. Lufaso, Unpublished work, 2011.
[43] X.- Zhou, L.R. Pederson, Q. Cai, J. Yang, B.J. Scarfino, M. Kim, W.B. Yelon, W.J. James, H.U. Anderson, C. Wang, J. Appl. Phys. 99 (2006) 08M918.
[44] J. Rodriguez-Carvajal, M. Hennion, F. Moussa, A.H. Moudden, L. Pinsard, A. Revcolevschi, Phys. Rev. B 57 (1998) R3189.